



**HAL**  
open science

## Decoding the IRX– $\beta$ dust attenuation relation in star-forming galaxies at intermediate redshift

M. Hamed, F. Pistis, M. Figueira, K. Malek, A. Nanni, V. Buat, A. Pollo, D. Vergani, M. Bolzonella, J. Krywult, et al.

► **To cite this version:**

M. Hamed, F. Pistis, M. Figueira, K. Malek, A. Nanni, et al.. Decoding the IRX– $\beta$  dust attenuation relation in star-forming galaxies at intermediate redshift. *Astronomy and Astrophysics - A&A*, 2023, 679, pp.A26. 10.1051/0004-6361/202346976 . hal-04505689

**HAL Id: hal-04505689**


**<https://hal.science/hal-04505689>**

Submitted on 16 Mar 2024

**HAL** is a multi-disciplinary open access archive for the deposit and dissemination of scientific research documents, whether they are published or not. The documents may come from teaching and research institutions in France or abroad, or from public or private research centers.

L'archive ouverte pluridisciplinaire **HAL**, est destinée au dépôt et à la diffusion de documents scientifiques de niveau recherche, publiés ou non, émanant des établissements d'enseignement et de recherche français ou étrangers, des laboratoires publics ou privés.

# Decoding the IRX– $\beta$ dust attenuation relation in star-forming galaxies at intermediate redshift

M. Hamed<sup>1</sup> , F. Pistis<sup>1</sup>, M. Figueira<sup>1,4</sup>, K. Małek<sup>1,2</sup>, A. Nanni<sup>1,5</sup>, V. Buat<sup>2</sup>, A. Pollo<sup>1,3</sup>, D. Vergani<sup>6</sup>, M. Bolzonella<sup>6</sup>, Junais<sup>1</sup>, J. Krywult<sup>7</sup>, T. Takeuchi<sup>8</sup>, G. Riccio<sup>1</sup>, and T. Moutard<sup>2</sup>

<sup>1</sup> National Centre for Nuclear Research, ul. Pasteura 7, 02-093 Warszawa, Poland  
e-mail: mahmoud.hamed@ncbj.gov.pl

<sup>2</sup> Aix Marseille Univ. CNRS, CNES, LAM, Marseille, France

<sup>3</sup> Astronomical Observatory of the Jagiellonian University, ul. Orła 171, 30-244 Krakow, Poland

<sup>4</sup> Institute of Astronomy, Faculty of Physics, Astronomy and Informatics, UMK, ul. Grudziądzka 5, 87-100 Toruń, Poland

<sup>5</sup> INAF – Osservatorio astronomico d’Abruzzo, Via Maggini SNC, 64100 Teramo, Italy

<sup>6</sup> INAF – Osservatorio di Astrofisica e Scienza dello Spazio di Bologna, Via Piero Gobetti 93/3, 40129 Bologna, Italy

<sup>7</sup> Institute of Physics, Jan Kochanowski University, ul. Świętokrzyska 15, 25-406 Kielce, Poland

<sup>8</sup> Division of Particle and Astrophysical Science, Nagoya University, Furo-cho, Chikusa-ku, Nagoya, Aichi 464-8602, Japan

Received 23 May 2023 / Accepted 24 August 2023

## ABSTRACT

**Aims.** We aim to understand what drives the IRX– $\beta$  dust attenuation relation at intermediate redshifts ( $0.5 < z < 0.8$ ) in star-forming galaxies. We investigate the role of various galaxy properties in shaping this observed relation.

**Methods.** We used robust [O II] $\lambda$ 3727, [O III] $\lambda$ 4959, 5007, and H $\beta$  line detections of our statistical sample of 1049 galaxies to estimate the gas-phase metallicities. We derived key physical properties that are necessary to study galaxy evolution, such as the stellar masses and the star formation rates, using the spectral energy distribution fitting tool CIGALE. Equivalently, we studied the effect of galaxy morphology (mainly the Sérsic index  $n$  and galaxy inclination) on the observed IRX– $\beta$  scatter. We also investigated the role of the environment in shaping dust attenuation in our sample.

**Results.** We find a strong correlation with respect to the IRX– $\beta$  relation on the gas-phase metallicity in our sample, as well as a strong correlation with galaxy compactness characterized by the Sérsic indexes. With higher metallicities, galaxies move along the track of the IRX– $\beta$  relation towards higher IRX. Correlations are also seen with the stellar masses, specific star formation rates, and the stellar ages of our sources. Metallicity is strongly correlated with the IRX– $\beta$  scatter, which also results from the presence of older stars and higher masses at higher beta values. Galaxies with higher metallicities show higher IRX and beta values. The correlation with specific dust mass strongly shifts the galaxies away from the IRX– $\beta$  relation towards lower  $\beta$  values. We find that more compact galaxies go through a greater amount of attenuation than less compact galaxies. There is a subtle variation in the dust attenuation scatter between edge-on and face-on galaxies, but the difference is not statistically significant. Galaxy environments do not significantly affect dust attenuation in our sample of star-forming galaxies at intermediate redshift.

**Key words.** galaxies: evolution – galaxies: ISM – galaxies: photometry – galaxies: star formation – ultraviolet: galaxies – infrared: galaxies

## 1. Introduction

The field of extragalactic astronomy has witnessed major developments over the last few decades with respect to the observation and understanding of the physical and chemical processes that control the evolution of galaxies. This understanding has resulted from interpretations of the ever-growing plethora of panchromatic data, which have provided unprecedented constraints on the interplay among the various components that make up galaxies. With powerful infrared (IR) telescopes such as the *Herschel* Space Observatory, it has become possible to better constrain the direct and indirect stellar emission of galaxies at higher redshifts, thereby expanding our knowledge beyond the highly resolved Local Universe.

In such complex systems as galaxies, different components interact with each other on different timescales. Such interactions include the dust attenuation of stellar light, which influences the total spectra of galaxies. Dust affects the shape of the spectral

energy distribution (SED) in a way that no other component does, despite its low contribution to the overall mass of the baryonic matter. Interstellar dust absorbs a significant amount of ultraviolet (UV) and optical radiation, then heating it up and re-emitting it at longer wavelengths, mostly in the far-infrared (FIR). As a consequence, part of the stellar UV emission becomes extinct, making it necessary to account for the missing radiation, especially when estimating key properties that describe the evolution of galaxies, such as star formation rates (SFRs). The derivation of SFR should rely on both UV-optical measurements and on the FIR emission (e.g., Blain et al. 2002; Takeuchi et al. 2005; Chapman et al. 2005; Hopkins & Beacom 2006; Madau & Dickinson 2014; Magnelli et al. 2014; Bourne et al. 2017; Whitaker et al. 2017; Gruppioni et al. 2020). Dust attenuation laws are used to correct the absorption of the short wavelength photons in order to recover fundamental properties of galaxies. This is typically done by assuming certain dust distribution relative to the dimmed stellar populations. Attenuation laws rely on the well studied dust

extinction in nearby galaxies (e.g., Calzetti et al. 1994, 2000; Charlot & Fall 2000; Johnson et al. 2007), and they are widely applied when reproducing the UV-optical spectra at different redshifts (for an extensive review on attenuation laws, see Salim & Narayanan 2020).

At higher redshifts, challenging measurements of FIR emission are overpowered by the readily available rest-frame UV emission data (e.g., Burgarella et al. 2007; Daddi et al. 2007; Bouwens et al. 2012). In turn, this limits the wavelength range from which the physical properties are inferred; therefore, a correct understanding of physical processes that prevail in the short wavelength domain, such as dust attenuation, becomes critical. Calzetti et al. (1994) showed a correlation between the UV spectral slope  $\beta$ , which is indicative of attenuation, measured with different spectral windows, and the Balmer optical depth of local starburst galaxies. Using the same sample, Meurer et al. (1995, 1999) found a tight relation between the heavily-attenuated  $\beta$  and the IR excess (IRX) of galaxies defined as the ratio between the IR and FUV luminosities  $\log(L_{\text{IR}}/L_{\text{FUV}})$ . This became known as the IRX- $\beta$  relation, since observed subsequently in numerous studies at low and high redshifts (e.g., Overzier et al. 2011; Boquien et al. 2012; Takeuchi et al. 2012; Buat et al. 2012; Cullen et al. 2017; Calzetti et al. 2021; Schouws et al. 2022).

Ideally, such a relation can be used to infer the FIR luminosity and affiliated properties of galaxies from lone UV observations. However, outliers of the IRX- $\beta$  relation were found in several samples at different redshift ranges (e.g., Casey et al. 2014; Álvarez-Márquez et al. 2016; McLure et al. 2018). These outliers are typically ultraluminous IR galaxies (ULIRGs) that populate the region of higher IRX and lower  $\beta$  values. Moreover, in older works,  $\beta$  tends to be biased towards lower values due to the underestimated UV fluxes from the small aperture of International Ultraviolet Explorer (IUE) and this relation was therefore revisited using the fluxes from the Galaxy Evolution Explorer (GALEX; Takeuchi et al. 2010, 2012), subsequently shifting it to higher  $\beta$ . Furthermore, the interpretation of this relation is not fully understood, despite the numerous attempts to unveil the factors upon which it relies. The attenuation curve used to reproduce the observed short wavelengths, as well as the dust geometry model used for attenuation, were found to strongly affect the IRX- $\beta$  scatter (Boquien et al. 2009; Casey et al. 2014; Salmon et al. 2016; Salim & Boquien 2019). This non-universality of dust attenuation laws is a known feature of dust obscuration at different redshift ranges (e.g., Kriek & Conroy 2013; Buat et al. 2018, 2019; Hamed et al. 2021). Other dependencies of the IRX- $\beta$  relation include: the age of stellar populations (Popping et al. 2017; Reddy et al. 2018), molecular gas mass (Ferrara et al. 2017), and gas-phase metallicity (Reddy et al. 2018; Shivaiei et al. 2020).

The IRX- $\beta$  relation has been well studied in the Local Universe and at high redshift. In this work, we aim to answer the key question of what drives the IRX- $\beta$  relation at intermediate redshift for star-forming galaxies, setting the evolution of such a relation in the context of galaxy evolution. We made use of robust metallicity estimations, galaxy morphological quantities, and other physical properties, such as stellar mass, in order to understand the attenuation scatter and better understand this relation at intermediate redshift, which is still an area that otherwise remains poorly studied.

In this work, we use the definition of the  $\text{IRX} = \log(L_{\text{IR}}/L_{\text{FUV}})$ , as well as that of  $\beta = \frac{\log(F_{\text{NUV}}/F_{\text{FUV}})}{\log(\lambda_{\text{FUV}}/\lambda_{\text{NUV}})} - 2$ . This paper is structured as follows. In Sect. 2, we describe the data used in this work. In Sect. 3, we discuss the SED fitting

procedure and the derivation of key physical properties that govern galaxy evolution. In Sect. 3.4, we discuss the quality of our SED fitting procedure. In Sect. 5, we show the IRX- $\beta$  relation of our sample with its fit. We derive the gas-phase metallicities of our sample and discuss its effect on the IRX- $\beta$  scatter in Sect. 4. In Sect. 6, we discuss different physical properties that drive the IRX- $\beta$  scatter, along with details of the dependence on the galaxy environment in Sect. 7. Our conclusions are presented in Sect. 8. Throughout this paper, we adopt the stellar IMF of Chabrier (2003) and a  $\Lambda$ CDM cosmology parameters (WMAP7; Komatsu et al. 2011):  $H_0 = 70.4 \text{ km s}^{-1} \text{ Mpc}^{-1}$ ,  $\Omega_M = 0.272$ , and  $\Omega_\Lambda = 0.728$ .

## 2. Data

### 2.1. Spectroscopic data

The data used in this work come from the VIMOS Public Extragalactic Redshift Survey (VIPERS; Guzzo et al. 2014; Garilli et al. 2014; Scodreggio et al. 2018). VIPERS used the VIMOS spectrograph at the Very Large Telescope to measure redshifts for a large number of galaxies ( $\sim 90\,000$ ) in two fields covering a total of  $\sim 24 \text{ deg}^2$  at  $0.5 \leq z \leq 1.2$ . The VIPERS sample has a limiting magnitude of  $i_{\text{AB}} \leq 22.5 \text{ mag}$  to maximize the signal-to-noise ratios (S/Ns) of the spectra and to select galaxies below  $z = 1.2$  (Guzzo et al. 2014). Moreover, the color selection based on the  $u, g, r, i$  bands allowed us to remove galaxies below  $z = 0.5$ , with median redshift of 0.7 (Guzzo et al. 2014). Spectroscopic observations of VIPERS were collected using the low-resolution red (LR-Red) grism ( $\sim 5500\text{--}9500 \text{ \AA}$ ) and a spectral resolution  $R \sim 220$  (Scodreggio et al. 2018). VIPERS data reduction was performed via a fully automated pipeline (Garilli et al. 2014). Redshifts were estimated using the EZ code (Garilli et al. 2010) aided by the visual inspection. The redshift quality flag, described in detail in Garilli et al. (2014), Guzzo et al. (2014), has tentative (flag 1) to secure (flags 2 to 4, with at least 90% of confidence) redshift measurements.

For reliable redshift estimations (Scodreggio et al. 2018), we selected galaxies for which the redshift flag was  $3.0 \leq z_{\text{flag}} \leq 4.5$ , corresponding to a redshift confidence of  $>99\%$ . We also selected the VIPERS sample with a flag that provides measurements with the quality of the measurement of emission lines. This flag is a goodness of fit assessment (a thorough description is detailed in Pistis et al. 2022; Figueira et al. 2022). The flags of emission lines were well-checked to deliver good estimations of the line profile. This was done by applying certain criteria, such as minimizing the distance between the peak of the fit and the brightest pixel and constraining the fit amplitudes to not differ significantly from the observed emission (Pistis et al. 2022).

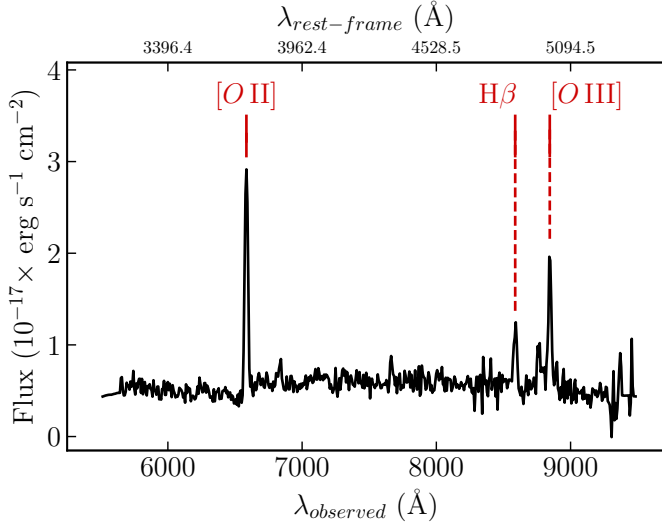
We used the penalized pixel fitting code (pPXF; Cappellari & Emsellem 2004) to model the VIPERS spectra by fitting stellar and gas templates from the MILES library (Vazdekis et al. 2010), as described in Pistis et al. (in prep.). A single Gaussian was used to fit each emission line of the gas component, yielding integrated fluxes and errors. Table 1 shows the median S/N values for the resulting four emission lines of our sample of galaxies. An example of the spectrum of a galaxy from our sample is shown in Fig. 1. Equivalent widths (EWs) and their errors were also computed.

### 2.2. Photometric data

The fields surveyed by VIPERS were previously mapped by the Canada-France-Hawaii Telescope Legacy Survey (CFHTLS), in

**Table 1.** S/N values of the detected lines for our sample.

Line	Median $S/N$
[O II] $\lambda$ 3727	21.79
H $\beta$	9.26
[O III] $\lambda$ 4959	3.38
[O III] $\lambda$ 5007	8.12


**Fig. 1.** Spectrum of a source from our sample (VIPERS ID: 105161086; HELP ID: J021747.792-055145.509) at  $z_{\text{spec}} = 0.766$ , highlighting the [O II] $\lambda$ 3727, [O III] $\lambda$ 4959,  $\lambda$ 5007, and H $\beta$  lines.

the optical range, with the wide photometric catalog T0007 release (Hudelot et al. 2012). The T0007 catalog with  $ugriz$  detections is an improvement of the initial T0005 and T0006 catalogs (Guzzo et al. 2014). In this newer catalog, the apparent magnitudes are given in the AB system and were corrected for Galactic extinction, with an extinction factor derived at the position of each galaxy using the dust maps of Schlegel et al. (1998). Near infrared magnitudes come from the  $Ks$  band detection of CFHT/WIRCam.

We required our sample to have detections in the FUV and NUV bands of the GALEX deep imaging survey. In the catalog of Moutard et al. (2016), GALEX data towards the CFHTLS-VIPERS fields were gathered, to measure the physical properties (e.g., SFR, stellar masses) of all galaxies in the VIPERS spectroscopic survey. The CFHTLS-T0007 maps were used as a reference to measure the  $Ks$ -band photometry, and the  $u$  band-selected sources were used as priors in estimating the redshift, as well as the FUV and NUV photometry.

Additionally, we extended the wavelength coverage to the FIR by cross-matching with the *Herschel* Extragalactic Legacy Project (HELP; Shirley et al. 2021) catalog, which provides a unique statistical data of IR detection of millions of galaxies detected at long wavelengths with *Herschel*, constructed homogeneously. To achieve the HELP catalog, *Herschel* fluxes were estimated using XID+ pipeline (Hurley et al. 2017), a probabilistic deblender of SPIRE maps which takes into account the positions of sources detected with *Spitzer* at 24  $\mu\text{m}$  (Duncan et al. 2018) from the Multiband Image Photometer (MIPS; Rieke et al. 2004). Detections from IRAC at its four channels from *Spitzer* were added to our data. We used data from

**Table 2.** Summary of photometric data in each band with its centered wavelength, mean of S/N, and the number of detections in our sample.

Telescope/ Instrument	Band	$\lambda$ ( $\mu\text{m}$ )	Median $S/N$	No. of detections
GALEX	FUV	0.15	5.45	1049
	NUV	0.23	9.78	1049
CFHT/MegaCam	$u$	0.38	31	1049
	$g$	0.49	61.69	1049
	$r$	0.63	50.62	1049
	$i$	0.76	78.69	1049
	$z$	0.89	40.90	1049
CFHT/WIRCam	$Ks$	2.14	25.25	1049
<i>Spitzer</i> /IRAC	Ch1	3.56	27.66	710
	Ch2	4.50	19.56	471
	Ch3	5.74	10.43	112
	Ch4	7.93	13.25	112
<i>Spitzer</i> /MIPS	MIPS1	24	15.90	116
	MIPS2	70	10.23	18
	MIPS3	160	6.19	3
<i>Herschel</i> /PACS	100 $\mu\text{m}$	102.62	1.30	592
	160 $\mu\text{m}$	167.14	1.38	592
<i>Herschel</i> /SPIRE	250 $\mu\text{m}$	251.50	2.63	592
	350 $\mu\text{m}$	352.83	1.51	592
	500 $\mu\text{m}$	511.60	1.05	592

the PACS instrument at 100 and 160  $\mu\text{m}$ , and from SPIRE at 250, 350, and 500  $\mu\text{m}$ .

### 2.3. Final sample

Apart from the redshift flag selection (discussed in Sect. 2.1), we also limited our sample to star-forming galaxies using the modified Baldwin, Phillips & Terlevich diagrams (BPT, Baldwin et al. 1981) by Lamareille (2010). This modified BPT diagram allows us to use the lines available in VIPERS, to discard active galactic nuclei (AGNs), low ionization nuclear emission regions (LINERs), and Seyfert sources.

The above-described selection yields a sample of 1049 galaxies, with their photometric S/Ns from Table 2, covering a redshift range of  $0.5 < z < 0.8$ . A total of 592 galaxies in our sample have FIR detections from the HELP catalog. All of the galaxies in our sample have spectroscopic redshifts. Table 2 shows the photometric bands used for our data and the associated S/N for our final sample.

Selection cuts were necessary to perform the analysis in this work, however, these resulted in few biases that needed to be taken into account. Here, we present the possible biases as well as their possible implications in our conclusions. The first selection to address is the selection of galaxies characterized by the strong emission lines, as those in the majority have the most reliable ( $\geq 99\%$  accuracy,  $3 < z_{\text{flag}} < 4.5$ ) redshift measurements in the VIPERS sample. Extremely dust obscured galaxies are removed with this cut, since their emission lines might be dim, as described in Scodreggio et al. (2018).

Furthermore, the selection on the quality of the lines was needed to select the galaxies that are considered to have reliable line measurement in VIPERS (e.g., Pistis et al. 2022; Figueira et al. 2022). Also, to compute metallicity using the  $R_{23}$  ratio, all three lines should be observed inside the spectral coverage of the instrument. For this reason we limited the sample

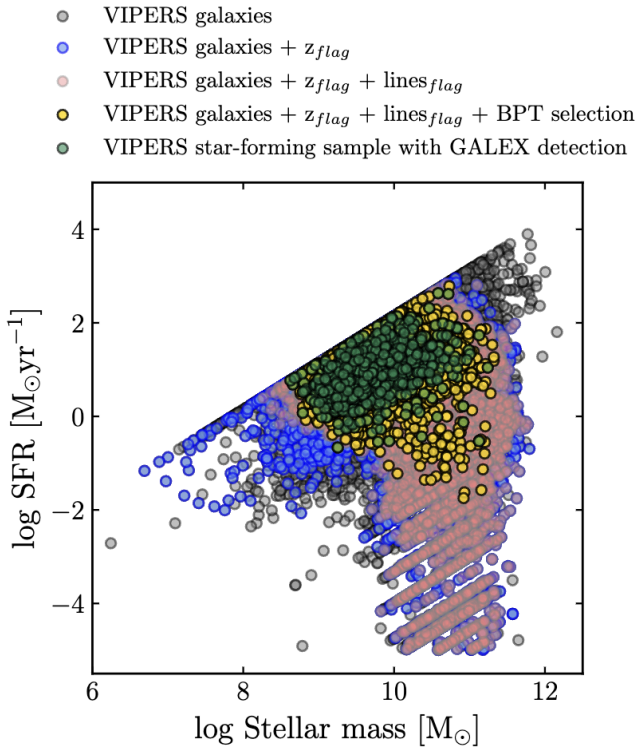


**Fig. 2.** Distribution of galaxies considered in this work throughout the selection process in the main sequence plane of star-forming galaxies. The SFRs and stellar masses in this plot were computed for the initial VIPERS catalog using HYPERZ (Bolzonella et al. 2000).

to redshift  $z_{\max} \sim 0.8$ . For the quality of lines of our galaxies (Pistis et al., in prep.; Garilli, priv. comm.), the line flags were taking into account the following criteria: the difference between the observed and Gaussian peak, the full width at half maximum (FWHM) of the line, difference between the observed and Gaussian amplitude, and S/N. We adopted the minimum requirement for our sample for the first three criteria (as detailed in Scodeggio et al. 2018; Pistis et al. 2022; Figueira et al. 2022; Pistis et al., in prep.) While we did not limit our sample to high S/N criteria on the emission lines, but the redshift flag did result in high S/N (presented in Table 1).

A key aspect of this work is to model the short wavelength fluxes of our sample in the most reliable way possible to derive the  $\beta$  values, as well as the attenuation values. Therefore, we required for the FUV and NUV detections to be available for our sample to avoid overfitting this slope. Additionally, for almost half of our sample, there were no available IR data; therefore we needed to rely on the energy balance of the SED models to estimate the IR luminosity of these objects. This required the highest coverage possible in the short wavelength to adopt, in the most correct way, the attenuation curve. This selection cut removes naturally the dusty and IR-bright sources. The selection on the BPT diagram was needed in order to reliably measure the IRX- $\beta$  relation for star-forming galaxies. Therefore, we did not consider passive galaxies in this work. The distribution of our sample in the main sequence of star-forming galaxies after every selection cut is presented in Fig. 2. In Fig. 2, the SFR and stellar mass values were estimated in the initial catalog using HYPERZ (Bolzonella et al. 2000; Davidzon et al. 2013). These cuts excluded the low mass galaxies, as well as passive ones.

**Table 3.** Steps of data selection and the size of our sample after each selection step.

Selection	Sample size
VIPERS sample	88 340
Redshift flag	53 680
Lines flag	36 850
BPT selection	6251
GALEX detection	1049

These selections and the resulting sample sizes after every cut are shown in Table 3.

### 3. Estimating physical properties from spectral energy distribution

To model the spectra of our galaxies, we first assumed a stellar population. We then attenuated this stellar population with dust, assuming different dust and star distributions. Also, we included the line measurements from the [O II] $\lambda$ 3727, [O III] $\lambda$ 4959,  $\lambda$ 5007, and H $\beta$  lines in the SED fitting procedure in CIGALE (Boquien et al. 2019) as done in Villa-Vélez et al. (2021). In the following subsections, we describe the different aspects of our SED fitting strategy and the motivation of our choice of certain templates and parameters.

#### 3.1. The stellar population and its formation history

To model the stellar emission and the spectral evolution of galaxies, we considered stars with different ages and a certain metallicity. In this work, we used the stellar population library of Bruzual & Charlot (2003), a solar metallicity and an IMF of Chabrier (2003), which takes into account a single star IMF as well as a binary star systems. In terms of modeling, star formation histories (SFH) are very sensitive to many complex factors including galaxy environments and merging, as well as gas accretion and its depletion (e.g., Elbaz et al. 2011; Ciesla et al. 2018; Schreiber et al. 2018; Pearson et al. 2019). The SFHs have a significant effect on fitting the UV part of the SED, consequently affecting the derived physical parameters such as the stellar masses and the SFRs. Initially, we tested different SFH models to fit the observed short wavelength photometry of our sources. These included a simple exponentially decreasing star formation characterized by an e-folding time,  $\tau$ , and a similar delayed model with a recent exponential burst or quench episode (Ciesla et al. 2017). In our models, we gave the e-folding time of the main stellar population ( $\tau_{\text{main}}$ ) a wide range of variation. Our initial results did not favor a recent burst in our sample, therefore, we proceeded to use the simpler delayed SFH. In this star formation scenario, a galaxy has built the majority of its stellar population in its earlier evolutionary phase, then the star formation activity slowly decreases over time. The SFR evolution over time is hereby modeled with:

$$\text{SFR}(t) \propto \frac{t}{\tau^2} e^{-t/\tau}, \quad (1)$$

where it translates into a delayed SFH slowed by the factor of  $\tau^2$ , the e-folding time of the main stellar population, and extended over the large part of the age of the galaxy. This SFH provided better fits compared to the one with the recent burst. We varied  $\tau$  (as shown in Table 4) to give a comprehensive flexibility of the delayed formation of the main stellar population.

**Table 4.** Input parameters of the important physical models used to fit the SEDs of our sample with CIGALE.

Parameter	Values
Star formation history	
Delayed	
Stellar age [Gyr]	Equally-spaced 32 values in [0.5, 8]
e-folding time ( $\tau$ ) [Gyr]	Equally-spaced 22 values in [0.5, 6]
Dust attenuation laws <sup>(a)</sup>	
(Calzetti et al. 2000)	
Color excess of young stars $E(B - V)$ mag	10 values in [0.1, 1]
Color excess of old stars ( $f_{\text{att}}$ )	0.1, 0.3, 0.5, 0.8, 1.0
(Charlot & Fall 2000)	
V-band attenuation in the ISM ( $A_V^{\text{ISM}}$ ) mag	30 values in [0.3–3]
$A_V^{\text{ISM}}/(A_V^{\text{BC}} + A_V^{\text{ISM}})$	0.1, 0.3, 0.5, 0.8, 1
Power law slope of the ISM	-0.7
Power law slope of the BC	-0.7
Dust emission	
(Draine et al. 2014)	
Mass fraction of PAH	1.12, 2.50, 3.90, 5.26, 6.63
Minimum radiation field ( $U_{\text{min}}$ )	1, 5, 15, 25, 35
Power law slope ( $\alpha$ )	2
Dust fraction in PDRs ( $\gamma$ )	5 values in [0.01, 0.2]

**Notes.** <sup>(a)</sup>One attenuation law was used at a time in the SED fitting procedures. Both approaches were used in order to derive accurate physical properties.

### 3.2. Dust attenuation

Modeling dust attenuation is an indispensable priority in any panchromatic SED fitting to reproduce the short wavelength photometry and, thus, to extract accurate physical properties. In this work, we used two contrasting approaches of attenuation laws for our SED fitting: the approach of Calzetti et al. (2000) and of Charlot & Fall (2000). While these two attenuation approaches are relatively simple, they differ with respect to the way a given stellar population is attenuated. Recently, Buat et al. (2019), Hamed et al. (2021) showed that for statistical samples, it is necessary to use these two attenuation laws in order to recover the physical properties of galaxies, choosing the best fit model among the two.

The attenuation curve of Calzetti et al. (2000) is a screen dust model. It was tuned to fit a sample of starbursts in the Local Universe, which represent high redshift UV-bright galaxies. This curve attenuates a stellar population with a simple power-law:

$$k(\lambda) = \frac{A(\lambda)}{E(B - V)}, \quad (2)$$

where  $k(\lambda)$  is the attenuation curve at a certain wavelength,  $A(\lambda)$  is the extinction curve, and  $E(B - V)$  is the color excess between the  $B$  and  $V$  bands.

Despite its simplicity, this attenuation curve is widely used in the literature (e.g., Burgarella et al. 2005; Buat et al. 2012, 2018; Małek et al. 2014, 2017; Pearson et al. 2017; Elbaz et al. 2018; Ciesla et al. 2020). However, it does not always succeed in reproducing the UV extinction of galaxies at higher redshifts (Noll et al. 2009; Lo Faro et al. 2017).

Another approach is to consider the dust spatial distribution relative to the stellar population. This is the core of the attenuation curve of Charlot & Fall (2000). In this approach, dust is considered to attenuate the dense and cooler stellar birth clouds (hereafter BCs) differently than ambient diffuse interstel-

lar media (ISM). This configuration is expressed by two independent power laws:

$$A(\lambda)_{\text{ISM}} \propto \left(\frac{\lambda}{\lambda_V}\right)^{\delta_{\text{ISM}}} \quad \text{and} \quad A(\lambda)_{\text{BC}} \propto \left(\frac{\lambda}{\lambda_V}\right)^{\delta_{\text{BC}}}, \quad (3)$$

where  $\delta_{\text{ISM}}$  and  $\delta_{\text{BC}}$  are the slopes of attenuation in the ISM and the BCs, respectively. Young stars that are in the BCs will therefore be attenuated twice: by the surrounding dust and additionally by the dust in the diffuse ISM. CF00 found that  $\delta_{\text{ISM}} = \delta_{\text{BC}} = -0.7$  satisfied dust attenuation in nearby galaxies, however, this curve is frequently used at higher redshifts (e.g., Małek et al. 2018; Buat et al. 2018; Salim & Narayanan 2020; Donevski et al. 2020; Hamed et al. 2021). By attenuating at higher wavelengths (until the NIR) more efficiently than the recipe of Calzetti et al. (2000), this approach considers a more attenuated older stellar population. This is due to the fact that the double power-law attenuation recipe of Charlot & Fall (2000) attenuates the ISM and the BC separately, where the ISM is assumed to contain the older stars. This attenuation curve, as a consequence, is shallower in the optical-to-NIR wavelength range than that of Calzetti et al. (2000), and this might produce slightly larger stellar masses (Małek et al. 2018; Buat et al. 2019; Hamed et al. 2021, 2023). To model the dust attenuation of the galaxies of our sample, we used the aforementioned laws, with the parameters presented in Table 4.

### 3.3. Dust emission

The modeling of dust emission of our sample is not only crucial to derive the key observables that govern galaxy evolution such as the SFRs. However, it is a cornerstone in correctly deriving IR luminosities, which, in turn, might affect the estimation of the IRX. To reproduce the IR emission in our SED models, we used the templates of Draine et al. (2014). These templates take into consideration different sizes of grains of carbon and silicate,

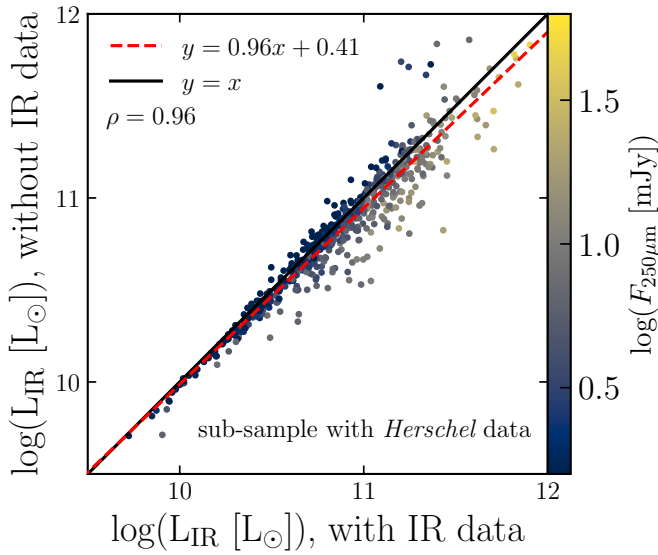


**Fig. 3.** Dust luminosities estimated for the IR-detected sub-sample (592 galaxies out of 1049), with and without IR data. The solid black line shows the one-to-one relation. The dashed red line shows the best fit of this comparison, and  $\rho$  is the Pearson coefficient. The scatter is color-coded with the fluxes of the sub-sample at 250  $\mu\text{m}$ .

thus allowing for different temperatures among the dust grains. These templates rely on observations and are widely used in the literature to fit FIR SEDs (e.g., [Buat et al. 2019](#); [Burgarella et al. 2020](#); [Hamed et al. 2021](#)).

Given that  $\sim 56\%$  of our sample possess FIR data from the HELP catalog, we fit these IR-detected galaxies with [Draine et al. \(2014\)](#) dust templates, with and without IR data. That is to say, in one fitting, we used the full available panchromatic photometric coverage from FUV to 500  $\mu\text{m}$ , using a stellar population library, SFH, dust attenuation, and dust emission templates. In another fitting procedure, we used the same templates to fit only the selected range of photometry from the FUV to IRAC4 band (8  $\mu\text{m}$ ). We then compared the dust luminosities estimated using these two techniques (this comparison is provided in Fig. 3). In this figure, the sources are color-coded with the intensity of the flux at 250  $\mu\text{m}$ . We notice that the IR luminosities estimated solely on the energy balance based on the UV-NIR detections are slightly underestimated for IR brighter objects. Although the gradient of the change is not large ( $0.2 < \log(F_{250\mu\text{m}} [\text{mJy}]) < 1.7$ ), the IR luminosities derived from the energy balance for the galaxies that miss IR detections may be slightly overestimated. Similar results were observed for the same test in [Małek et al. \(2018\)](#) for star-forming galaxies with the redshift ranging from  $0.5 < z < 2$ , as well as for dusty star-forming galaxies at  $z \sim 2$  in [Buat et al. \(2019\)](#), and in [Junais et al. \(2023\)](#) for low- and high-surface-brightness galaxies. In order to estimate the IR luminosities of the objects in Fig. 3, the best attenuation law that describes each source was used, based on the reduced  $\chi^2$ .

The obtained IR luminosities with the aforementioned techniques correlated with a Pearson coefficient of  $\rho = 0.96$ . We then proceeded with fitting the photometry of galaxies that do not possess IR observations in the HELP catalog (457 galaxies out of 1049) with the same input parameters of [Draine et al. \(2014\)](#) templates, computing the IR luminosities based on the energy balance applied in the SED fitting using the short wavelength data. This allows for a reliable estimation of IR luminosities. We show the

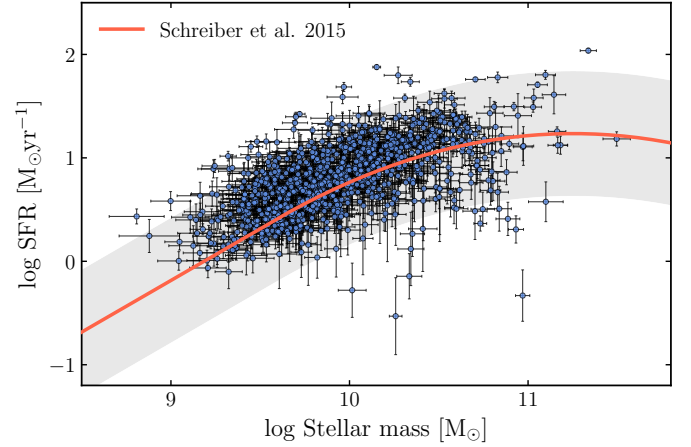


**Fig. 4.** Star formation rates for our sample fitted with the best attenuation curve against stellar masses. The red line shows the main sequence of star-forming galaxies from [Schreiber et al. \(2015\)](#) at  $z = 0.6$  (median for our sample).

star-forming galaxy main sequence of our sample in Fig. 4. Our fitting technique provided an overall low uncertainties of physical properties, such as the stellar masses and the SFR.

#### 3.4. SED quality and model assessment

To test the reliability of our SED models, we used CIGALE to generate a mock galaxy sample and fit the SEDs with the same methods applied to our sample. We build the mock catalog by perturbing the fluxes of our best SEDs with errors sampled from a Gaussian distribution with a standard deviation equivalent to the uncertainty observed in the real fluxes. We show the mock analysis of the important estimated quantities in Fig. 5, where we give a comparison between the real physical properties that we derived for our sample and their mock equivalents. The mean  $\chi^2_{\text{reduced}}$  of our sample was 8.6, mainly due to the large error bars of the IR data. For each galaxy, we selected the attenuation law that best describes its observed photometry by comparing their  $\chi^2$ , as in [Buat et al. \(2019\)](#), [Hamed et al. \(2021\)](#).

To estimate  $\beta$  for each galaxy in our sample, we fit a power-law function to the SED of each galaxy between the rest-frame ranges 0.126  $\mu\text{m}$  and 0.260  $\mu\text{m}$ . IRX was estimated directly from the SED fitting process, by dividing the IR luminosity by the FUV luminosity for each source, that is,  $\text{IRX} = \log(L_{\text{IR}}/L_{\text{FUV}})$ .

We also compared the SFRs derived using the spectroscopic lines, notably the H $\beta$  and O II lines, with the ones obtained using SED of the photometry. We show this comparison in Appendix A. This ensures a coherent interpretation of the SFR using the different methods. Overall, the mock analysis showed that our estimations of the physical observables, such as dust luminosities, SFRs, stellar masses, and IRX and  $\beta$ , are reliable.

#### 4. Estimating the metallicity

Different calibrations are often used in the literature to measure the gas phase metallicity based on different line ratios ([Pilyugin 2001](#); [Tremonti et al. 2004](#); [Nagao et al. 2006](#); [Curti et al. 2017](#)). Making use of the robust oxygen emission lines along the H $\beta$  line, we measured the gas phase metallicity using the ratio:

$$R_{23} = \frac{[\text{O II}]\lambda 3727 + [\text{O III}]\lambda \lambda 4959, 5007}{\text{H}\beta} \quad (4)$$

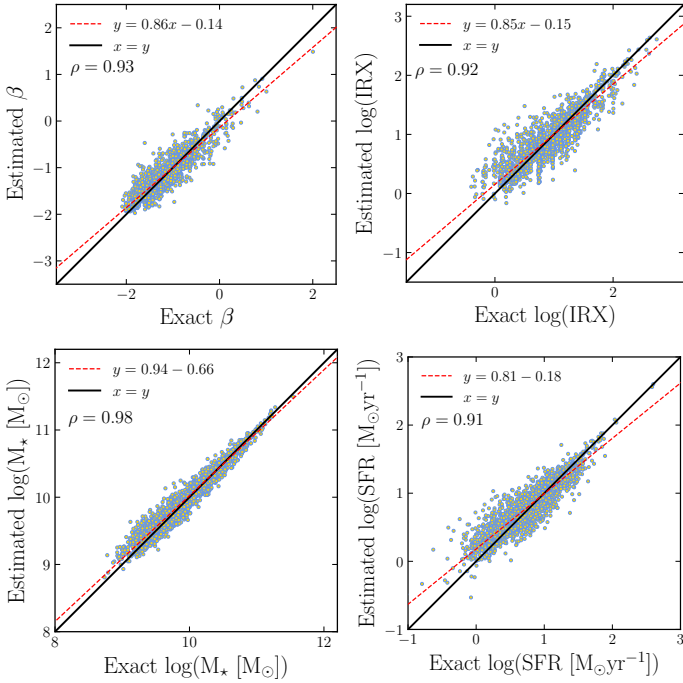


**Fig. 5.** Comparison between some of the true parameters of the mock SEDs and the results from the SED modeling with CIGALE. The “exact” values are from mock models and  $\rho$  is the Pearson coefficient.

The  $R_{23}$  ratio was initially proposed in [Pagel et al. \(1979\)](#), and since then its tuning to oxygen abundance was improved by various photoionization models ([Nagao et al. 2006](#)). To derive the metallicity of our galaxies, we used the calibration proposed by [Tremonti et al. \(2004\)](#), which is based on the  $R_{23}$  ratio of star-forming galaxies of double-valued  $R_{23}$ -abundance ratios. Following [Nagao et al. \(2006\)](#) we verified whether our sample is in the upper branch ( $[\text{O III}]\lambda 5007/[\text{O II}]\lambda 3727 < 2$ ) and found that all data of our sample belong to the upper branch. Additionally, we removed all the sources that fall below the calibration limit of  $12 + \log(\text{O}/\text{H}) \leq 8.4$ , since this metallicity calibration is valid for values above that threshold. This discarded 47 galaxies, leaving a total of 1002 galaxies for which valid metallicity estimations were calculated.

The calibration proposed by [Tremonti et al. \(2004\)](#) estimates the metallicity from theoretical model fitting of emission-lines. The model fits were calculated by combining SSP synthesis models from [Bruzual & Charlot \(2003\)](#) and CLOUDY photoionization models ([Ferland et al. 1998](#)). The relation between metallicity and  $R_{23}$  is given by:

$$12 + \log(\text{O}/\text{H}) = 9.185 - 0.313x - 0.264x^2 - 0.321x^3, \quad (5)$$

where  $x \equiv \log R_{23}$ .

To estimate the metallicities of our sample using the aforementioned lines, we corrected the lines for attenuation. The value of attenuation  $A_{(V,\text{stellar})}$  was computed via the SED fitting. We then passed from  $A_{(V,\text{stellar})}$  to  $A_{(V,\text{nebular})}$  assuming factor ( $f = 0.57$ ) as proposed in [Rodríguez-Muñoz et al. \(2022\)](#). To correct each line for attenuation we applied the law described in [Cardelli et al. \(1989\)](#).

## 5. IRX– $\beta$ relation of our sample

We show the scatter of IRX– $\beta$  of our sample of star-forming galaxies in [Fig. 6](#). This scatter is observed to be higher than

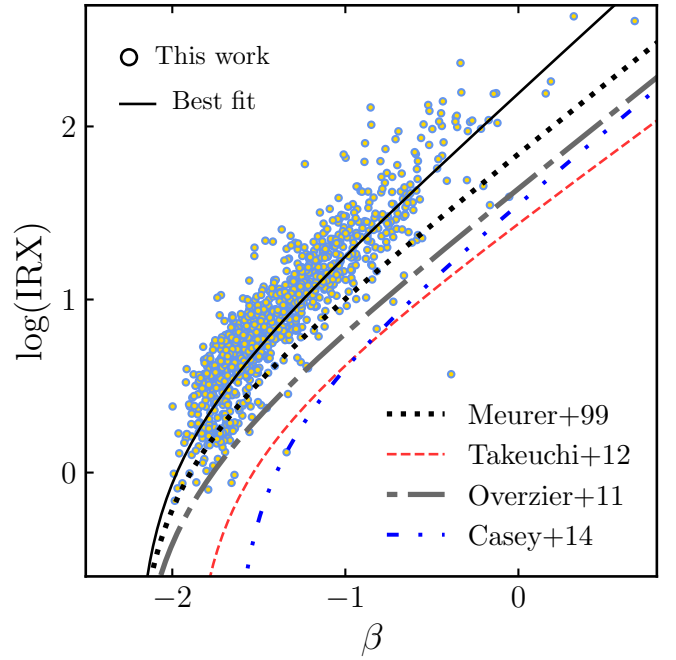


**Fig. 6.** IRX– $\beta$  scatter of our sample. The original [Meurer et al. \(1999\)](#) fit is shown in dotted line. We also make a comparison with the fits from [Overzier et al. \(2011\)](#), [Takeuchi et al. \(2012\)](#), [Casey et al. \(2014\)](#), denoted with grey dashed-dotted, red dashed, and dashed-double-dotted lines, respectively. The solid black line shows Eq. (9), describing our sample.

the relation fitted on the sample of local starburst galaxies by [Meurer et al. \(1999\)](#). We fit the scatter of our sample in the IRX– $\beta$  diagram following the same method presented in [Hao et al. \(2011\)](#) and used similarly in [Boquien et al. \(2012\)](#).

To separate the influence of the SFH from the attenuation, we connect the attenuation to  $\beta$ :

$$A_{\text{FUV}} = (\beta - \beta_0) \times c_\beta, \quad (6)$$

where  $A_{\text{FUV}}$  is the attenuation in the FUV band,  $\beta_0$  is the intrinsic UV slope (without dust), and  $c_\beta$  is the attenuation constant connecting both sides of the equation. The former can be seen as the degree to which the attenuation in the FUV band is influenced by the reddening caused by dust. On the other hand, IRX can be linked with dust attenuation via:

$$A_{\text{FUV}} = 2.5 \times \log(1 + c_{\text{IRX}} 10^{\text{IRX}}), \quad (7)$$

where  $c_{\text{IRX}}$  is the proportion of emission in the FUV band relative to the attenuation observed in other bands ([Meurer et al. 1999](#); [Boquien et al. 2012](#)). Equations (6) and (7) can be integrated as in [Hao et al. \(2011\)](#):

$$\text{IRX} = \log\left(\frac{10^{0.4 \times (\beta - \beta_0) c_\beta} - 1}{c_{\text{IRX}}}\right). \quad (8)$$

For our sample, this leads to the following equation:

$$\text{IRX} = \log[(10^{0.91\beta + 2.02} - 1)/0.67]. \quad (9)$$

Our fitted relation lies above the relation given originally by [Meurer et al. \(1999\)](#), and the subsequent work on the same sample by [Takeuchi et al. \(2012\)](#). Our relation is 0.22 dex higher



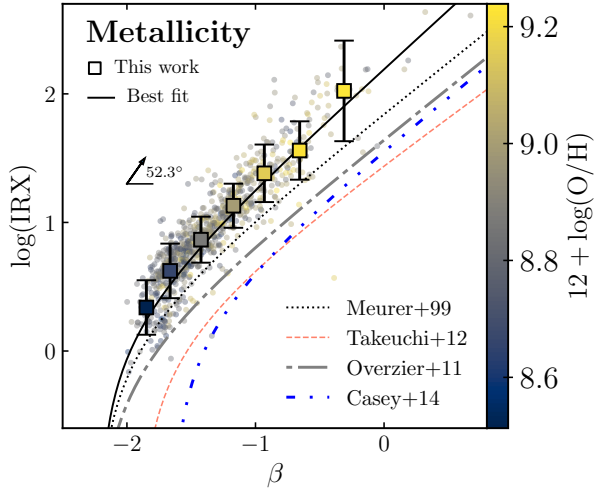


**Fig. 7.** IRX– $\beta$  scatter of our sample color-coded with metallicity. Points denote the VIPERS sample binned by  $\beta$ , every bin contains the same number of galaxies (160 galaxies), except the last bin (containing 89 galaxies). The best fits from the literature and the best fit of our sample are also shown. Colors and line-styles of these fits are the same as in Fig. 6. The arrow represents the trend of the metallicity, based on the scattered distribution (the direction is from the mean of the bottom 30th percentile of the distribution of metallicity to that of the top 70th percentile). The angle is between the arrow and the  $x$  axis.

on average than that of Meurer et al. (1999), with a mean difference of 0.11 dex for  $-2.2 < \beta < -0.8$  and 0.33 dex for  $-0.8 < \beta < -0.6$ . This can be attributed to different factors, such as the larger sample size in our work (the Meurer+99 sample was made up of 44 galaxies, while that of Takeuchi et al. (2012) was 57 starburst galaxies) to the larger dynamical range of properties that our sample exhibits, or simply different redshift range that probe different epochs of Universe. For instance, Meurer+99 had only four data points at  $\beta > -0.5$ , and all of them are in the Local Universe. Although slightly higher, our sample represents the normal star-forming galaxies at intermediate redshift, unlike the aforementioned works which studied primarily local UV-bright starbursts. Additionally, our sample might have higher specific dust masses than that of local galaxies, which helps in shifting our sources towards bluer beta and slightly higher IRX. Our fitted relation falls in between the ones derived for the local starbursts on the one hand, and the high redshift dusty star-forming galaxies on the other hand (Álvarez-Márquez et al. 2016,  $2 < z < 3.5$ , McLure et al. 2018,  $2 < z < 3$ , Safarzadeh et al. 2017,  $z = 0$  and  $2 < z < 3$ ). Also, the fact that we applied the best attenuation law that describes every galaxy in our sample has a natural impact on the loci of these galaxies in the IRX– $\beta$  plane (Boquien et al. 2012). The IRX– $\beta$  relation was shown to be related to the geometry of dust and stars (Boquien et al. 2009, 2012; Narayanan et al. 2018; Liang et al. 2021). Therefore, we consider our fit to be representative of the normal star-forming galaxies at intermediate redshift.

## 6. Results and discussion: Considering how physical properties are correlated with the IRX– $\beta$ relation

### 6.1. Correlation with metallicity

A correlation between dust reddening and gas-phase metallicity is expected, as metals in the ISM will be depleted onto the

same dust grains that attenuate the young stars and their emission lines. This means that the more metal content present in the ISM, the more dust grains will be formed. Our findings suggest that metallicity is a significant contributing factor to the variability observed in the IRX– $\beta$  relation, as shown in Fig. 7. Metallicity is indicative of the characteristics of small dust particles that affects the attenuation curve (Zelko & Finkbeiner 2020). Lower gas-phase metallicity results in stronger UV radiation in the ISM, leading to the breaking down of larger dust grains into smaller particles, assuming a conservation of mass of dust. This results in an increase of the overall attenuation (Shivaei et al. 2020). Other works (e.g., Conroy et al. 2010; Wild et al. 2011) have also found that higher gas-phase metallicity is indicative of higher dust attenuation.

Although higher dust-mass galaxies occupied the upper part of the scatter, the correlation was not net (as it is with the metallicity). Therefore, dust mass was not found to be a key factor in the diagram. However, we found that dust-to-star geometry was strongly responsible in moving the scatter to the right (Popping et al. 2017). Galaxies that preferred the attenuation curve of CF00 were located towards redder  $\beta$  (higher  $\beta$  values).

### 6.2. Correlation with other galaxy properties

We show the dependence of the IRX– $\beta$  relation with the physical properties of our sample in Fig. 8. Higher mass galaxies with older stellar population occupy the higher IRX and  $\beta$  values of the diagram. The Pearson coefficients between the stellar mass and IRX and  $\beta$  are found to be  $\rho = 0.96$  and  $\rho = 0.98$ , respectively, for our sample, signifying a strong correlation. This almost linear scaling between the stellar mass and IRX and  $\beta$  was also found at different redshift ranges (e.g., Koprowski et al. 2018; Shivaei et al. 2020).

On the other hand, the specific SFR ( $sSFR = \log SFR/M_\star$ ) is found to decrease at higher  $\beta$ . This decrease is found to be stronger with  $\beta$  rather than IRX. The  $sSFR$  can be seen as a competition between the SFR and the stellar mass. At higher  $\beta$  values, the sharper increase of the stellar mass overcomes the slow increase in the SFR of our sample. Generally, high SFR in galaxies, with higher dust masses, results in a larger fraction of young massive stars in the stellar population, which increases the UV radiation. This UV radiation is absorbed by dust, which re-emits in in the IR causing a higher IRX value.

The attenuation in the  $V$  band shows a strong trend in the diagram, with more optically attenuated galaxies located in the higher IRX and high  $\beta$  values. The specific dust mass ( $M_{\text{dust}}/M_\star$ ) correlation with IRX– $\beta$  is shown in Fig. 8 (middle right panel). With a higher specific dust mass, galaxies move away from the fitted relation towards lower  $\beta$  values.

### 6.3. Variation with morphology

The morphological parameters of our sample were estimated using GALFIT in Krywult et al. (2017), where the authors applied Sérsic profiles fitting over the  $r$ -band of CFHT in their sample of VIPERS galaxies. A full description of the methodology used in deriving morphological parameters is detailed in Krywult et al. (2017). We notice a strong correlation between the Sérsic index ( $n$ ) and the distribution of our sample in the IRX– $\beta$  diagram. the Sérsic index gives a Pearson coefficient of 0.95 with both IRX and  $\beta$  separately. We show the correlation with the Sérsic index in Fig. 8 (lower right panel). The number of sources in this particular plot is lower than in the other plots of IRX– $\beta$ , because we applied the most secure flag of Sérsic profiles

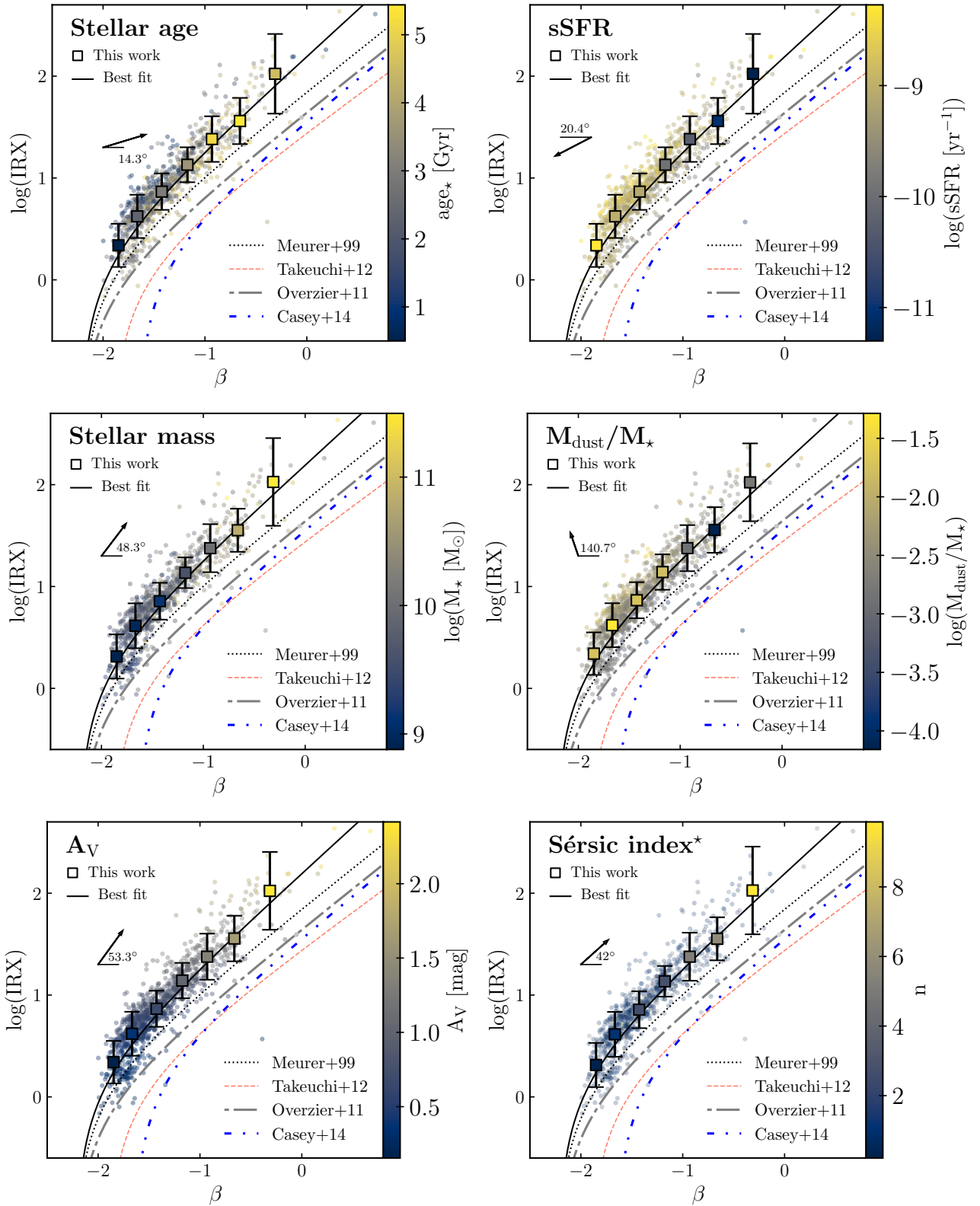


**Fig. 8.** IRX- $\beta$  binned scatter of our sample color-coded with different physical properties. Squares denote the VIPERS sample binned by  $\beta$ , every bin contains the same number of galaxies (160 galaxies), except the last bin (containing 89 galaxies). The original Meurer et al. (1999) fit is shown in dotted line. We also compare with fits from Overzier et al. (2011), Takeuchi et al. (2012), Casey et al. (2014), denoted with grey dashed-dotted, red dashed, and dashed-double-dotted lines, respectively. The solid black line shows Eq. (9), describing our sample. The arrows represent the direction of the trend, starting from the mean of the bottom 30th percentile of the distribution up to that of the top 70th percentile of a given quantity, they are meant to show the general direction of the trend. The lower right figure with the Sérsic index, a total of 823 galaxies (instead of 1049) are binned, due to GALFIT flag selection, based on Krywult et al. (2017). The angles are between the arrows and the x or y axis.

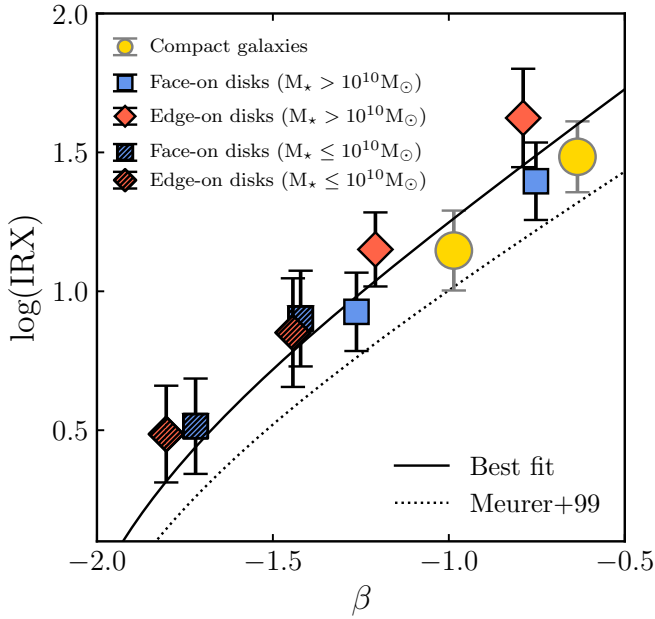


**Fig. 9.** Our sample binned by  $\beta$ . Yellow circles represent compact galaxies ( $n > 2$ ). Blue squares show face-on disks ( $b/a > 0.5$  and  $n < 2$ ). Red diamonds represent edge-on disk galaxies ( $b/a < 0.5$  and  $n < 2$ ). Full markers show the higher mass galaxies in our sample, that is  $M_* > 10^{10} [M_\odot]$ . While the hatched markers are that of the lower mass sources, that is,  $M_* \leq 10^{10} [M_\odot]$ .

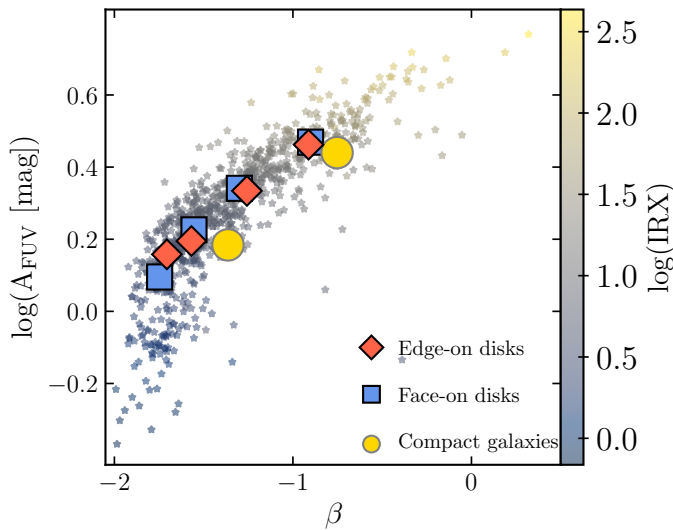


**Fig. 10.** Variation in the attenuation in FUV with  $\beta$ , color-coded with  $\log(\text{IRX})$ . Edge-on disks have  $b/a < 0.5$  and  $n < 2$ , while face-on disks have  $b/a > 0.5$  and  $n < 2$ . Compact galaxies are those for which  $n > 2$ .

fitting. This flag discards the galaxies for which GALFIT did not converge and keeps galaxies with  $0.2 < n < 10$ . This effectively discarded 226 sources from our sample and left 823 galaxies out of 1049 remaining. Our results show a strong correlation of the loci of our galaxies in the  $\text{IRX}-\beta$  diagram with galaxy compactness in the optical band.

Equivalently, we studied the variation of the loci of galaxies in the  $\text{IRX}-\beta$  scatter with the same galaxy inclination as in Wang et al. (2018). We used the same definition of disk galaxy inclinations as in the literature: galaxies for which the ratio of minor to major axis ( $b/a$ )  $> 0.5$  are classified as face-on galax-

ies. On the other hand, galaxies whose  $b/a \leq 0.5$  are considered edge-on galaxies. These definitions are valid for disk sources ( $n < 2$ ). In our analysis, we also adopt the same notion of compact galaxies, as those for which  $n > 2$  (Wang et al. 2018). We show the  $\text{IRX}-\beta$  distribution of our sample based on galaxy morphology in Fig. 9, where every bin contains the same number of galaxies ( $\sim 110$  galaxies). Additionally, we separated the galaxies in our sample according to their stellar masses.

We find that compact galaxies ( $n > 2$ ) occupy the higher IRX values relative to the less compact ones. This is shown using the whole sample in Fig. 8 (lower right panel). However, for the disk sub-sample, we find that for galaxies whose stellar masses are  $M_* > 10^{10} [M_\odot]$  (259 sources), the IRX values are higher for edge-on galaxies than that of face-on galaxies. On the other hand, the lower mass galaxies ( $M_* \leq 10^{10} [M_\odot]$ ) show no preferential loci on the  $\text{IRX}-\beta$  diagram with inclination, as shown in Fig. 9, where similar results were shown in Wang et al. (2018). The higher IRX values for high-mass edge-on galaxies, might be caused by the increase of the optical depth in these sources compared to the face-on galaxies (Wang et al. 2018).

In Fig. 10, we show the variation of the attenuation in FUV with  $\beta$  for the different morphological classifications. For a fixed  $\beta$  value, we find no difference in attenuation between edge-on and face-on galaxies. This suggests that the inclination of galaxies does not affect the  $\text{IRX}-\beta$  scatter. A similar conclusion was reported in Wang et al. (2018).

## 7. Dust attenuation and galaxy environment

The density field of VIPERS data was computed by Cucciati et al. (2017), where the authors estimated the local environment around the galaxies. In their work, they computed the galaxy density contrast between the local density at a comoving distance around each source, and the mean density at a given redshift. The mean density was achieved using mock catalogs. The local density of each galaxy was measured based on its fifth nearest neighbour. The local density contrast is defined as (e.g., Siudek et al. 2022):

$$\delta(\text{RA}, \text{Dec}, z) = \frac{\rho(\text{RA}, \text{Dec}, z) - \overline{\rho(z)}}{\overline{\rho(z)}}, \quad (10)$$

where  $\rho(\text{RA}, \text{Dec}, z)$  is the local density of a given galaxy and  $\overline{\rho(z)}$  is the mean density at a redshift,  $z$ .

We separated galaxies that reside into overdense and underdense regions, defined as the 5th and 95th percentiles of the  $\log(1+\delta)$  distribution, respectively (shown in Fig. 11, left panel). We did this in order to see the subtle difference in the  $\text{IRX}-\beta$  diagram (Fig. 11, right panel). We find no significant correlation with the  $\text{IRX}-\beta$  relation. Even though the galaxies that reside in less dense environments are slightly shifted towards the higher  $\beta$  values, for a given  $\beta$ , IRX is similar in the two galaxy groups within the error bars.

We analyzed the attenuation in FUV bands of the galaxies from our sample with their environment overdensities. We show this in Fig. 12. We find no relation between the environment overdensities and dust attenuation. Galaxies' environments strongly affect their physical properties (e.g., Peng et al. 2010); however it is not yet understood how this might affect dust attenuation in galaxies. Shivaiei et al. (2020) drew a similar conclusion, namely, that environment does not seem to correlate with dust attenuation and, consequently, with the  $\text{IRX}-\beta$  relation. We extend this conclusion from the high redshift in their work down

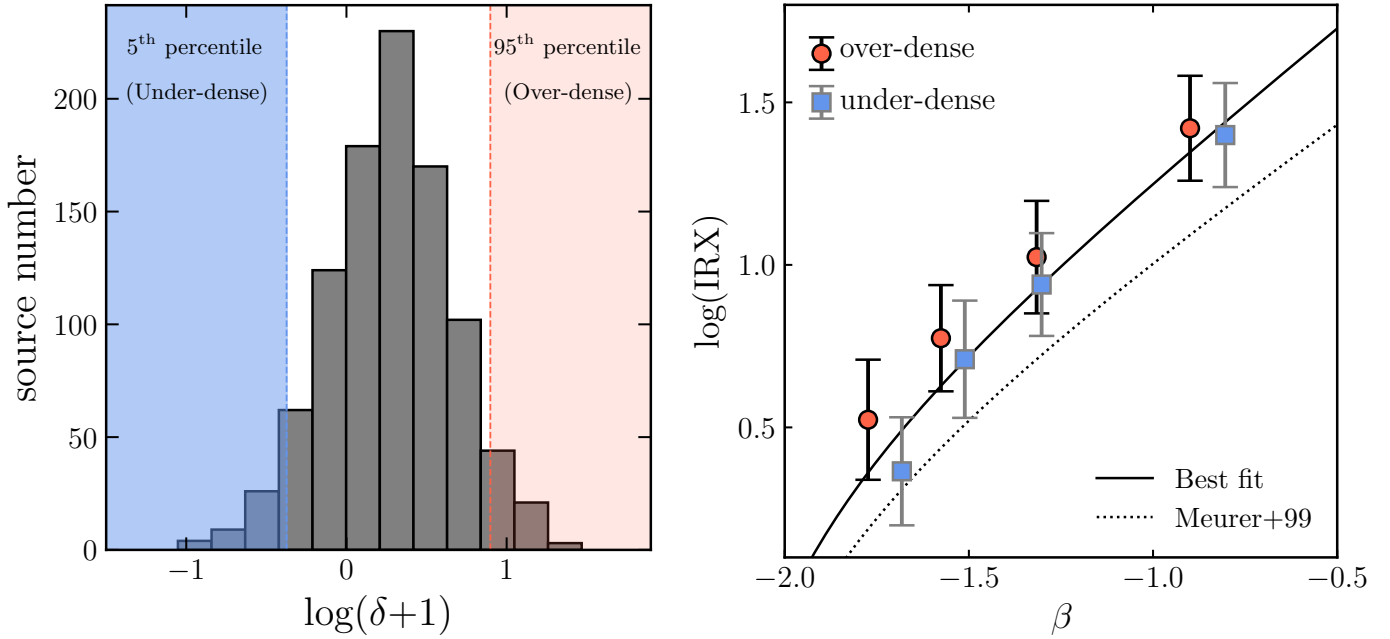


**Fig. 11.** Distribution of galaxy overdensity  $\log(\delta + 1)$  show in the left panel. In the blue region, we show the selection of the 5th percentile of the overdensity (the galaxies residing in less-dense environments), and in the red region the selection of the 95th percentile of the distribution (galaxies residing in overdense regions). Same percentiles of the selection from the left panel, but in the IRX- $\beta$  scatter.

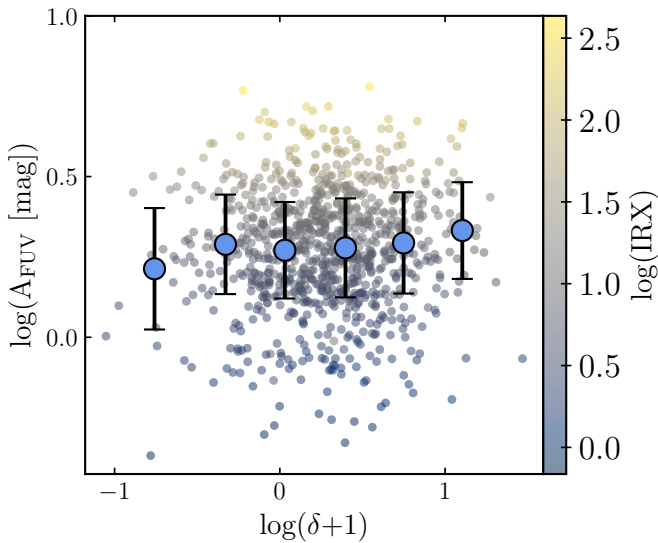


**Fig. 12.** Attenuation in the FUV band, as a function of galaxy overdensities. The scatter represents the galaxies color-coded with IRX. We show the binned values for the whole sample (170 galaxies per bin).

to intermediate redshift, showing that the variation of the  $A_{\text{FUV}}$  with galaxy overdensities is absent.

To quantify the degree of correlation in the IRX- $\beta$  diagram, we show in Fig. 8 the angles of the distribution of each physical property. We find that the most correlated quantities with the IRX- $\beta$  plane are: metallicities, galaxy compactness, and stellar mass.

## 8. Conclusions

In this work, we dissected the IRX- $\beta$  dust attenuation relation for a large sample of 1049 galaxies at intermediate redshift

( $0.5 < z < 0.8$ ). Having robust emission lines measurement at our disposal, specifically the  $H\beta$ ,  $O\text{II}$  and the double  $[\text{O III}]$  lines, we estimated the gas-phase metallicities of 1002 sources in our sample using the calibration from Tremonti et al. (2004). Additionally, having full FUV to FIR detections for about half of our sample, we were able to reliably compute the SEDs of the galaxies. We showed that for galaxies that do not possess FIR detections, we were able to reliably estimate the dust luminosity based on the SED energy balance principle.

Among the tested physical properties of our sample in the IRX- $\beta$  relation, the gas-phase metallicity correlated strongly with the loci of the galaxies within this diagram by moving the galaxies along the track of the relation, as was shown in Fig. 7. A strong trend was also found with the stellar masses of our galaxies and the age of their main stellar population. We conclude that metallicity strongly correlates with the IRX- $\beta$  scatter; this also results from presence of older stars and higher masses at higher beta values. Galaxies with higher metallicities show higher IRX and higher beta values. The sSFR was found to decrease at lower  $\beta$  values, due to the competition between SFR and stellar mass where the SFR were not high enough to compensate the clear increase of the stellar mass at higher IRX values. Similar results have been reported in the literature (e.g., Boquien et al. 2012; Koprowski et al. 2018; Shivaie et al. 2020). Our results suggest that at intermediate redshift, where earlier star-forming galaxies evolve through, the IRX- $\beta$  scatter remains dependent on these physical properties.

We notice that the correlation with the specific dust mass is strong in terms of shifting the galaxies farther away from the IRX- $\beta$  relation towards lower  $\beta$  values. This is due to the strong increase in the relative mass of dust compared to the stellar mass, leading to higher IR luminosities.

Having the morphological parameters of our sample (Krywult et al. 2017), we analyzed the effect that certain morphological properties have on the location of galaxies in the IRX- $\beta$  plane. We find a strong correlation with the Sérsic index

$n$ , that is, with higher IRX and  $\beta$  values, galaxy compactness seems to increase at the same rate. Morphologically, we find that more optically-compact objects (compact stellar population regions), witness a larger amount of attenuation than less compact galaxies.

We also tested the effect of galaxy inclination in the observed IRX– $\beta$  scatter, by separating our sample into edge-on disks, face-on disks and compact galaxies. Additionally, we split the sample into lower mass galaxies ( $M_{\star} \leq 10^{10} [M_{\odot}]$ ) and higher-mass galaxies ( $M_{\star} > 10^{10} [M_{\odot}]$ ). Similarly as in Wang et al. (2018), we find that for the higher mass sub-sample, IRX values were higher for edge-on disks. However, for the lower mass sub-sample, this variation is not noticeable. The increase in IRX values for edge-on higher mass galaxies could be attributed to the higher optical depth in these galaxies as compared to the face-on galaxies, as suggested by Wang et al. (2018). Checking the variation of the attenuation in the FUV band with  $\beta$ , we found no difference in the amount of attenuation and  $\beta$  with IRX, as shown in Fig. 10.

We studied the effect of galaxy environments on dust attenuation in Sect. 7. To do so, we took the 5th percentile and the 95th percentile of the distribution of our sample's overdensities (computed in Cucciati et al. 2017). By this, we checked the loci of galaxies that most reside in less dense environments and overdense ones. We found subtle difference in this relation, galaxies in over-dense environments were above the fitted IRX– $\beta$  relation (Eq. (9)), and galaxies in underdense regions were below this fit. However, given the large error bars, this difference was not robust. In a similar way, we tested the attenuation in the FUV bands of our galaxies depending on the overdensity of their environments in Fig. 12. We conclude that the environment does not affect the dust attenuation of our sample of star-forming galaxies at intermediate redshift, despite the known effect the environment has on main galaxy properties such as the SFRs (Peng et al. 2010). Similar results were reported by Shivaeei et al. (2020) around cosmic noon.

**Acknowledgements.** M.H. acknowledges the support by the National Science Centre, Poland (UMO-2022/45/N/ST9/01336). We thank the anonymous referee for the constructive report. K.M., M.H., and J. have been supported by the National Science Centre (UMO-2018/30/E/ST9/00082). A.N. acknowledges support from the Narodowe Centrum Nauki (UMO-2020/38/E/ST9/00077). A.P., F.P., and J.K. were supported by the Polish National Science Centre grant (UMO-2018/30/M/ST9/00757). This research was supported by Polish Ministry of Science and Higher Education grant DIR/WK/2018/12. M.H. thanks Médéric Boquien and Stéphane Arnouts for the discussion.

## References

- Álvarez-Márquez, J., Burgarella, D., Heinis, S., et al. 2016, *A&A*, 587, A122
- Baldwin, J. A., Phillips, M. M., & Terlevich, R. 1981, *PASP*, 93, 5
- Blain, A. W., Smail, I., Ivison, R. J., Kneib, J. P., & Frayer, D. T. 2002, *Phys. Rep.*, 369, 111
- Bolzonella, M., Miralles, J. M., & Pelló, R. 2000, *A&A*, 363, 476
- Boquien, M., Calzetti, D., Kennicutt, R., et al. 2009, *ApJ*, 706, 553
- Boquien, M., Buat, V., Boselli, A., et al. 2012, *A&A*, 539, A145
- Boquien, M., Burgarella, D., Roehlly, Y., et al. 2019, *A&A*, 622, A103
- Bourne, N., Dunlop, J. S., Merlin, E., et al. 2017, *MNRAS*, 467, 1360
- Bouwens, R. J., Illingworth, G. D., Oesch, P. A., et al. 2012, *ApJ*, 754, 83
- Bruzual, G., & Charlot, S. 2003, *MNRAS*, 344, 1000
- Buat, V., Noll, S., Burgarella, D., et al. 2012, *A&A*, 545, A141
- Buat, V., Boquien, M., Małek, K., et al. 2018, *A&A*, 619, A135
- Buat, V., Ciesla, L., Boquien, M., Małek, K., & Burgarella, D. 2019, *A&A*, 632, A79
- Burgarella, D., Buat, V., & Iglesias-Páramo, J. 2005, *MNRAS*, 360, 1413
- Burgarella, D., Le Flocc'h, E., Takeuchi, T. T., et al. 2007, *MNRAS*, 380, 986
- Burgarella, D., Nanni, A., Hirashita, H., et al. 2020, *A&A*, 637, A32
- Calzetti, D., Kinney, A. L., & Storchi-Bergmann, T. 1994, *ApJ*, 429, 582
- Calzetti, D., Armus, L., Bohlin, R. C., et al. 2000, *ApJ*, 533, 682
- Calzetti, D., Battisti, A. J., Shivaeei, I., et al. 2021, *ApJ*, 913, 37
- Cappellari, M., & Emsellem, E. 2004, *PASP*, 116, 138
- Cardelli, J. A., Clayton, G. C., & Mathis, J. S. 1989, *ApJ*, 345, 245
- Casey, C. M., Scoville, N. Z., Sanders, D. B., et al. 2014, *ApJ*, 796, 95
- Chabrier, G. 2003, *PASP*, 115, 763
- Chapman, S. C., Blain, A. W., Smail, I., & Ivison, R. J. 2005, *ApJ*, 622, 772
- Charlot, S., & Fall, S. M. 2000, *ApJ*, 539, 718
- Ciesla, L., Elbaz, D., & Fensch, J. 2017, *A&A*, 608, A41
- Ciesla, L., Elbaz, D., Schreiber, C., Daddi, E., & Wang, T. 2018, *A&A*, 615, A61
- Ciesla, L., Béthermin, M., Daddi, E., et al. 2020, *A&A*, 635, A27
- Conroy, C., Schiminovich, D., & Blanton, M. R. 2010, *ApJ*, 718, 184
- Cucciati, O., Davidzon, I., Bolzonella, M., et al. 2017, *A&A*, 602, A15
- Cullen, F., McLure, R. J., Khochfar, S., Dunlop, J. S., & Dalla Vecchia, C. 2017, *MNRAS*, 470, 3006
- Curti, M., Cresci, G., Mannucci, F., et al. 2017, *MNRAS*, 465, 1384
- Daddi, E., Dickinson, M., Morrison, G., et al. 2007, *ApJ*, 670, 156
- Davidzon, I., Bolzonella, M., Coupon, J., et al. 2013, *A&A*, 558, A23
- Davidzon, I., Cucciati, O., Bolzonella, M., et al. 2016, *A&A*, 586, A23
- Donevski, D., Lapi, A., Małek, K., et al. 2020, *A&A*, 644, A144
- Draine, B. T., Aniano, G., Krause, O., et al. 2014, *ApJ*, 780, 172
- Duncan, K. J., Brown, M. J. I., Williams, W. L., et al. 2018, *MNRAS*, 473, 2655
- Elbaz, D., Dickinson, M., Hwang, H. S., et al. 2011, *A&A*, 533, A119
- Elbaz, D., Leiton, R., Nagar, N., et al. 2018, *A&A*, 616, A110
- Ferland, G. J., Korista, K. T., Verner, D. A., et al. 1998, *PASP*, 110, 761
- Ferrara, A., Hirashita, H., Ouchi, M., & Fujimoto, S. 2017, *MNRAS*, 471, 5018
- Figueira, M., Pollo, A., Małek, K., et al. 2022, *A&A*, 667, A29
- Garilli, B., Fumana, M., Franzetti, P., et al. 2010, *PASP*, 122, 827
- Garilli, B., Guzzo, L., Scodreggio, M., et al. 2014, *A&A*, 562, A23
- Grupponi, C., Béthermin, M., Loiacono, F., et al. 2020, *A&A*, 643, A8
- Guzzo, L., Scodreggio, M., Garilli, B., et al. 2014, *A&A*, 566, A108
- Hamed, M., Ciesla, L., Béthermin, M., et al. 2021, *A&A*, 646, A127
- Hamed, M., Małek, K., Buat, V., et al. 2023, *A&A*, 674, A99
- Hao, C.-N., Kennicutt, R. C., Johnson, B. D., et al. 2011, *ApJ*, 741, 124
- Hopkins, A. M., & Beacom, J. F. 2006, *ApJ*, 651, 142
- Hudlot, P., Cuillandre, J. C., Withington, K., et al. 2012, *VizieR Online Data Catalog: II/317*
- Hurley, P. D., Oliver, S., Betancourt, M., et al. 2017, *MNRAS*, 464, 885
- Johnson, B. D., Schiminovich, D., Seibert, M., et al. 2007, *ApJS*, 173, 392
- Junais, Małek, K., Boissier, S., et al. 2023, *A&A*, 676, A41
- Kennicutt, R. C., Jr. 1998, *ARA&A*, 36, 189
- Komatsu, E., Smith, K. M., Dunkley, J., et al. 2011, *ApJS*, 192, 18
- Koprowski, M. P., Coppin, K. E. K., Geach, J. E., et al. 2018, *MNRAS*, 479, 4355
- Kriek, M., & Conroy, C. 2013, *ApJ*, 775, L16
- Krywult, J., Tasca, L. A. M., Pollo, A., et al. 2017, *A&A*, 598, A120
- Lamareille, F. 2010, *A&A*, 509, A53
- Liang, L., Feldmann, R., Hayward, C. C., et al. 2021, *MNRAS*, 502, 3210
- Lo Faro, B., Buat, V., Roehlly, Y., et al. 2017, *MNRAS*, 472, 1372
- Madau, P., & Dickinson, M. 2014, *ARA&A*, 52, 415
- Magnelli, B., Lutz, D., Saintonge, A., et al. 2014, *A&A*, 561, A86
- Małek, K., Pollo, A., Takeuchi, T. T., et al. 2014, *A&A*, 562, A15
- Małek, K., Bankowicz, M., Pollo, A., et al. 2017, *A&A*, 598, A1
- Małek, K., Buat, V., Roehlly, Y., et al. 2018, *A&A*, 620, A50
- McLure, R. J., Dunlop, J. S., Cullen, F., et al. 2018, *MNRAS*, 476, 3991
- Meurer, G. R., Heckman, T. M., Leitherer, C., et al. 1995, *AJ*, 110, 2665
- Meurer, G. R., Heckman, T. M., & Calzetti, D. 1999, *ApJ*, 521, 64
- Moutard, T., Arnouts, S., Ilbert, O., et al. 2016, *A&A*, 590, A102
- Nagao, T., Maiolino, R., & Marconi, A. 2006, *A&A*, 459, 85
- Narayanan, D., Davé, R., Johnson, B. D., et al. 2018, *MNRAS*, 474, 1718
- Noll, S., Burgarella, D., Giovannoli, E., et al. 2009, *A&A*, 507, 1793
- Overzier, R. A., Heckman, T. M., Wang, J., et al. 2011, *ApJ*, 726, L7
- Pagel, B. E. J., Edmunds, M. G., Blackwell, D. E., Chun, M. S., & Smith, G. 1979, *MNRAS*, 189, 95
- Pearson, W. J., Wang, L., van der Tak, F. F. S., et al. 2017, *A&A*, 603, A102
- Pearson, W. J., Wang, L., Alpaslan, M., et al. 2019, *A&A*, 631, A51
- Peng, Y.-J., Lilly, S. J., Kovač, K., et al. 2010, *ApJ*, 721, 193
- Pilyugin, L. S. 2001, *A&A*, 374, 412
- Pistis, F., Pollo, A., Scodreggio, M., et al. 2022, *A&A*, 663, A162
- Popping, G., Somerville, R. S., & Galametz, M. 2017, *MNRAS*, 471, 3152
- Reddy, N. A., Oesch, P. A., Bouwens, R. J., et al. 2018, *ApJ*, 853, 56
- Rieke, G. H., Young, E. T., Engelbracht, C. W., et al. 2004, *ApJS*, 154, 25
- Rodríguez-Muñoz, L., Rodighiero, G., Pérez-González, P. G., et al. 2022, *MNRAS*, 510, 2061
- Safarzadeh, M., Hayward, C. C., & Ferguson, H. C. 2017, *ApJ*, 840, 15
- Salim, S., & Boquien, M. 2019, *ApJ*, 872, 23
- Salim, S., & Narayanan, D. 2020, *ARA&A*, 58, 529
- Salmon, B., Papovich, C., Long, J., et al. 2016, *ApJ*, 827, 20

- Schlegel, D. J., Finkbeiner, D. P., & Davis, M. 1998, [ApJ](#), 500, 525
- Schouws, S., Stefanon, M., Bouwens, R., et al. 2022, [ApJ](#), 928, 31
- Schreiber, C., Pannella, M., Elbaz, D., et al. 2015, [A&A](#), 575, A74
- Schreiber, C., Glazebrook, K., Nanayakkara, T., et al. 2018, [A&A](#), 618, A85
- Scodeggio, M., Guzzo, L., Garilli, B., et al. 2018, [A&A](#), 609, A84
- Shirley, R., Duncan, K., Campos Varillas, M. C., et al. 2021, [MNRAS](#), 507, 129
- Shivaei, I., Darvish, B., Sattari, Z., et al. 2020, [ApJ](#), 903, L28
- Siudek, M., Małek, K., Pollo, A., et al. 2022, [A&A](#), 666, A131
- Takeuchi, T. T., Buat, V., & Burgarella, D. 2005, [A&A](#), 440, L17
- Takeuchi, T. T., Buat, V., Heinis, S., et al. 2010, [A&A](#), 514, A4
- Takeuchi, T. T., Yuan, F.-T., Ikeyama, A., Murata, K. L., & Inoue, A. K. 2012, [ApJ](#), 755, 144
- Tremonti, C. A., Heckman, T. M., Kauffmann, G., et al. 2004, [ApJ](#), 613, 898
- Vazdekis, A., Sánchez-Blázquez, P., Falcón-Barroso, J., et al. 2010, [MNRAS](#), 404, 1639
- Villa-Vélez, J. A., Buat, V., Theulé, P., Boquien, M., & Burgarella, D. 2021, [A&A](#), 654, A153
- Wang, W., Kassin, S. A., Pacifici, C., et al. 2018, [ApJ](#), 869, 161
- Whitaker, K. E., Pope, A., Cybulski, R., et al. 2017, [ApJ](#), 850, 208
- Wild, V., Charlot, S., Brinchmann, J., et al. 2011, [MNRAS](#), 417, 1760
- Zelko, I. A., & Finkbeiner, D. P. 2020, [ApJ](#), 904, 38

## Appendix A: Comparison of SED-computed SFRs with tracers

We show in Figure A.1 the comparisons between the SFRs computed using CIGALE and those computed using the emission lines  $H\beta$  and O II. The correlation between all these estimators demonstrate the effectiveness of the derived SFRs using panchromatic SED fitting. To compute the SFRs from O II, we used the method described in Kennicutt (1998):

$$\log(\text{SFR}(\text{O II}) [\text{M}_{\odot}\text{yr}^{-1}]) = \log(L(\text{O II}) [\text{erg s}^{-1}]) - 41.20.$$

To compute the SFRs from  $H\beta$ , we assume  $H_{\alpha}/H_{\beta}=2.86$  (Figueira et al. 2022). Then, we computed the SFRs using the Kennicutt (1998) relation for  $H_{\alpha}$ , which is given by:

$$\log(\text{SFR}(H_{\alpha}) [\text{M}_{\odot}\text{yr}^{-1}]) = \log(L(H_{\alpha}) [\text{erg s}^{-1}]) - 41.10.$$

Both  $L(\text{O II})$  and  $H_{\beta}$  are corrected for attenuation, as described in Section 4.

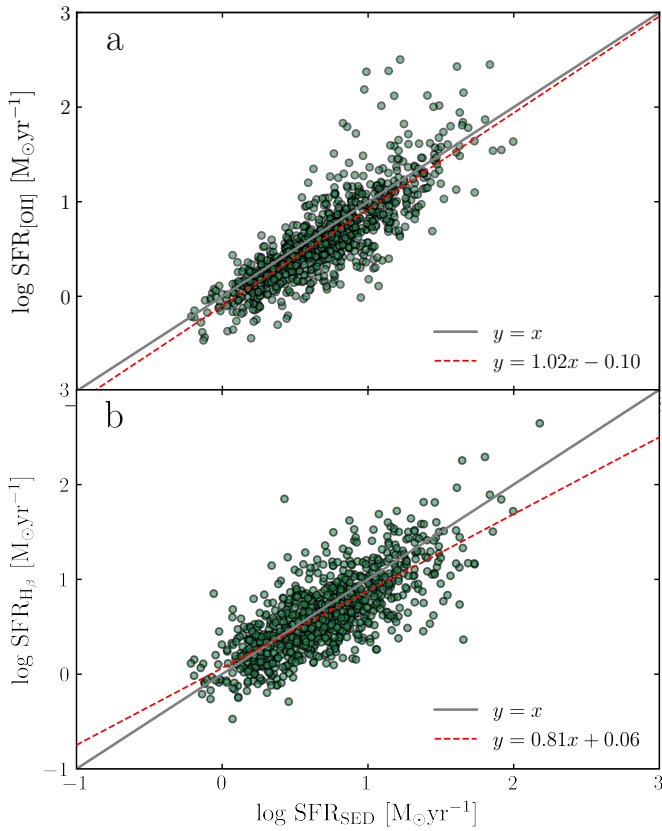


**Fig. A.1.** Comparison between star formation rates derived with (a): O II, (b):  $H_{\beta}$  with those derived with SED fitting. The red dashed line is the best fit of the distribution.

## Appendix B: Mass-complete sub-sample

We also derive the IRX- $\beta$  relation for our mass-complete sub-sample. To achieve the mass-complete sub-sample, we select galaxies for which  $\log(M_{\star}) \geq 10.18 \text{ M}_{\odot}$  for  $z \leq 0.6$ , and  $\log(M_{\star}) \geq 10.47 \text{ M}_{\odot}$  for  $z \leq 0.8$ , following Davidzon et al. (2016) selections for VIPERS.

These selections result in only 258 galaxies from our initial sample. The IRX- $\beta$  fit for this sub-sample is then given by:

$$\text{IRX} = \log[(10^{2.98\beta+1.95} - 1)/0.64]. \quad (\text{B.1})$$

We show the fit for the mass-complete sub-sample in Figure B.1. The mass-complete sample is statistically less important than our full sample, and it lacks data in the lower IRX and  $\beta$  values, therefore it must be considered with caution.

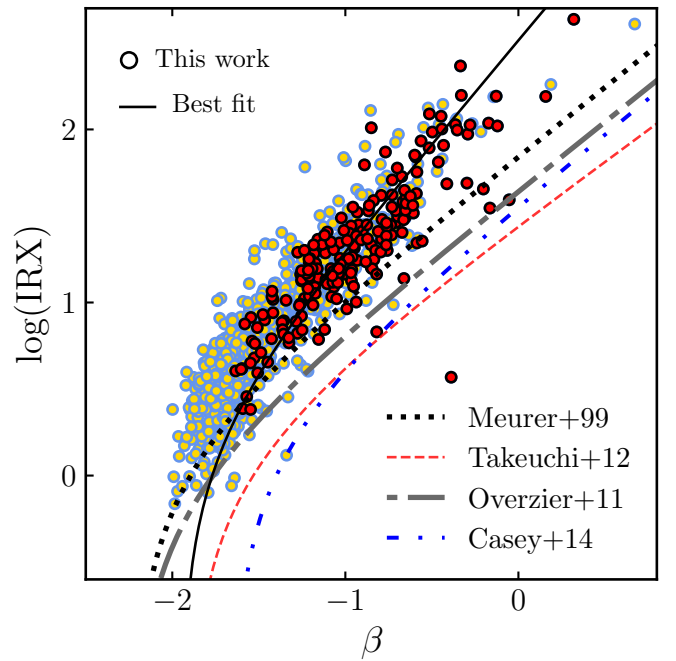


**Fig. B.1.** IRX- $\beta$  scatter of our sample. The original Meurer et al. (1999) fit is shown in dotted line. We also compare with fits from Overzier et al. (2011), Takeuchi et al. (2012), Casey et al. (2014), denoted with grey dashed-dotted, red dashed, and dashed-double-dotted lines, respectively. The solid black line shows Equation B.1, describing our mass-complete sample. Red dots denote the mass-complete sub-sample in this work.